ORIGINAL PAPER

CrossMark

Flower-like ZnO/ionic liquid composites: structure, morphology, and photocatalytic activity

Letícia G. da Trindade [1,2] · Letícia Zanchet [2] · Aline B. Trench [1] · Josiane Carneiro Souza [1] · Maria H. Carvalho [3] ·
Adilson J. A. de Oliveira [3] · Ernesto C. Pereira [1] · Tatiana M. Mazzo [4] · Elson Longo [1]

Abstract

Two ionic liquids (ILs) with different alkyl chains, 1-butyl-3-methylimidazolium chloride (BMI.Cl) and 1-hexadecyl-3-methylimidazolium chloride (C16MI.Cl), were incorporated into ZnO particles using the microwave-assisted hydrothermal (MAH) method. The morphology and microstructure of ZnO and ZnO/IL composites were characterized along with their photocatalytic effect for dye degradation. While the incorporation of ILs into the ZnO particles did not alter their morphology, it converted the shallow defects into deep defects. These changes improved Rhodamine B (RhB) photodegradation efficiency. The dye degradation reached 62% when ZnO/C1640 was used, whereas it reached 30% when pure ZnO was used, during the same time interval.

Keywords ZnO · Ionic liquid · Optical properties · Photocatalysis

Introduction

Industrial development and population growth cause significant damage to the environment, especially water pollution. Among the main water pollutants, organic dyes stand out because they are toxic and harmful to underwater life and humans and are very difficult to be biodegraded [1, 2]. While Rhodamine B (RhB) is one of the most commonly used organic dyes in the textile and food industries [3], it is harmful and toxic to humans and animals and is a known carcinogen [4, 5]. Therefore, many methods have been developed to

✉ Letícia G. da Trindade
  leticiagt@terra.com.br

1 Chemistry Department—CDMF/LIEC, UFSCar, P.O. Box 676, São Carlos, SP 13560-970, Brazil

2 Institute of Chemistry, UFRGS, P.O. Box 15003, Porto Alegre 91501-970, Brazil

3 Physics Department, UFSCar, P.O. Box 676, São Carlos, SP 13565-905, Brazil

4 Institute of Marine Sciences, Federal University of São Paulo (UNIFESP), P.O. Box 11070-100, Santos, SP, Brazil

eliminate organic dyes from water sources. Among them, photocatalytic degradation is an effective method to reduce toxic and waste materials like organic dyes [6–8]. Different chemical compounds, such as SnO_2, ZrO_2, CdS, ZnS, TiO_2, and ZnO, have been suggested as photocatalysts for the degradation of organic dyes under UV or solar light [9–14]. Among them, ZnO is regarded as a promising option due to its high photosensitivity, non-toxic character, low cost, environmental friendliness, and ease of availability [15–17]. However, due to its high band gap (3.3 eV), ZnO absorbs light in the UV region and has a high recombination rate of photogenerated charges (electron/hole pairs), which decreases the photocatalytic efficiency of the process, rendering it unsuitable as commercial photocatalyst [18, 19]. Therefore, the challenge is to alter the structure of ZnO for improved efficiency under solar light excitation [20]. One of the most efficient ways of altering the structure of ZnO is controlling the morphology of the material, since it strongly influences its photocatalytic performance [21, 22].

Byzynski et al. [23] obtained ZnO and ZnO:N samples using the modified polymeric precursor (MPP) and microwave-assisted hydrothermal (MAH) methods. The samples were tested for RhB degradation under UV and visible light for 2 h at 25 °C. They observed that all ZnO samples presented photocatalytic activity for both conditions; however, samples synthesized using the MAH method presented a

higher photocatalytic activity when compared with samples obtained by MPP. The MAH samples exhibited superior performance because they did not promote the recombination of as many electron/hole pairs as the MPP samples did. Moreover, the MAH method, due to the anisotropic growth mechanism, promoted the formation of nanorod particles where the major crystal faces exposed their (101) and (100) plane surfaces, while the MPP method formed nanoplate particles with preferred (001) and (100) crystal faces exposure.

Recently, ionic liquids (ILs) have been used as co-solvents or co-surfactants to fabricate inorganic materials due to properties, such as negligible vapor pressure, high thermal stability, good dissolving ability, and high ionic conductivity [24–27]. Incorporating ILs into materials can reduce the size of grains, which is beneficial for improving some properties, such as photocatalytic activity [28].

In this work, we present the incorporation of two ILs, 1-butyl-3-methylimidazolium chloride (BMI.Cl) and 1-hexadecyl-3-methylimidazolium chloride (C16MI.Cl), into flower-like ZnO particles. The effects of the sizes of the alkyl chains and amount of IL on the structure of ZnO materials were studied. The photocatalytic abilities of ZnO materials were assessed for RhB degradation under visible light.

Experimental section

Synthesis

We prepared ZnO particles using the MAH method. First, 0.03 mol L^{-1} Zn $(NO_3)_2$ was dissolved in 50 mL of deionized water under constant stirring. After that, 50 mL of 2.0 mol L^{-1} KOH solution was added. This mixture was transferred to a reactor and heated in a Panasonic® modified microwave oven, model MN-S46B, with a frequency of 2450 MHz and 1050 W power. The reactor was heated to 140 °C, and the temperature was maintained for 32 min. After cooling, the reaction products were washed with deionized water to pH 7 and oven-dried for 12 h at 60 °C.

The structural formulas of BMI.Cl and C16MI.Cl are shown in Fig. 1, and their syntheses followed the procedure described in the literature [29].

The incorporation of ILs into the ZnO particles occurred as follows: 0.20 g ZnO or 0.20 g ZnO containing 20 or 40% by mass of respective ILs was mixed with 1.0 mL ethanol, and the mixture was sonicated for 30 min. Subsequently, 0.5 mL deionized water was added, and the mixture was sonicated for another 30 min. After that, the mixture was placed into an oven at 250 °C for 1 h. Details on the compositions and designations of the samples are presented in Table 1.

Characterization of the materials

The obtained powders were investigated using X-ray diffraction (XRD), micro-Raman spectroscopy, N_2 adsorption-desorption isotherm measurements, field-emission gun-scanning electron microscopy (FEG-SEM), transmission electron microscopy (TEM), ultraviolet–visible (UV–Vis) absorption spectroscopy, photoluminescence (PL) spectroscopy, photocatalytic degradation, attenuated total reflectance Fourier transform infrared (ATR-FTIR) spectroscopy, and X-ray photoelectron spectroscopy (XPS).

The XRD analyses were performed utilizing a Rigaku detector with Cu Kα radiation (λ = 0.15406 nm) in the 2θ range of 5 to 120° using 0.02° min^{-1} steps. Rietveld refinements [30] were performed using GSAS-EXPGUI software [31]. Micro-Raman spectroscopy was carried out using an iHR550 spectrometer (Horiba Jobin-Yvon, Japan) coupled to a charge-coupled device detector and an argon-ion laser (Melles Griot, United States) operating at 514.5 nm with maximum power of 200 mW. The spectra were measured in the 100–1000 cm^{-1} range. The specific surface areas, porosities, and average pore diameters were obtained using N_2 adsorption-desorption isotherm measurements employing a TriStar II 3020 V 1.03 instrument. The samples were preheated at 120 °C for 8 h in a vacuum before each measurement. The specific surface area was determined using the Brunauer–Emmett–Teller (BET) method at − 196 °C, at a partial pressure $P/P_0 < 1$. The pore size distribution was calculated using the N_2 adsorption-desorption isotherms and the classic theoretical model of Barrett, Joyner, and Halenda (BJH). Surface morphologies were studied utilizing FEG-SEM data using a ZEISS model 105 DSM940A spectrometer operating at 10 keV. TEM images were performed using a FEI Tecnai
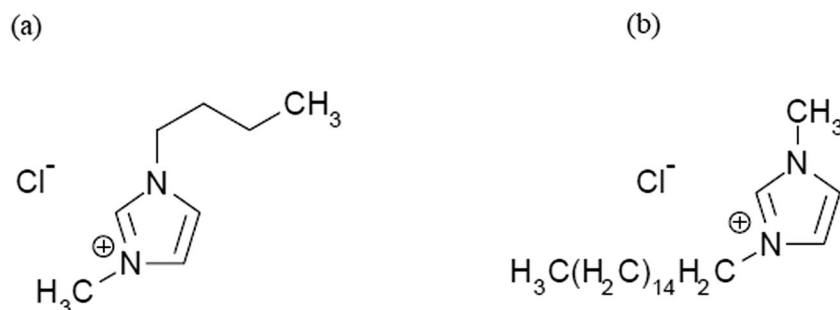
Fig. 1 Structural formulas of a BMI.Cl and b C16MI.Cl

(a)

(b)

Table 1 Composition and designation of samples

Sample	Mass of ZnO (g)	Ionic liquid	Ionic liquid (wt.%)
ZnO	0.20	–	–
ZnO/C420	0.20	BMI.Cl	20
ZnO/C440	0.20	BMI.Cl	40
ZnO/C1620	0.20	C16MI.Cl	20
ZnO/C1640	0.20	C16MI.Cl	40

F20 (Netherlands) microscope operating at 200 kV. The UV–Vis absorption spectra were recorded using the total diffuse reflectance mode of a Cary 5G (Varian, USA) spectrophotometer. We performed PL measurements in the 350 to 850 nm range using a Thermal Jarrel-Ash Monospec 27 cm monochromator, and a Hamamatsu R955 photomultiplier A Coherent Innova 200 krypton ion laser with a 350.7 nm (2.57 eV) exciting wavelength was used. The laser output was maintained at 500 mW and became 14 mW when reaching the sample.

The photocatalytic activities of the ZnO and ZnO/IL samples were tested for RhB degradation in aqueous solutions under visible radiation. We dispersed 50 mg samples in aqueous solutions of RhB (50 mL of a $1 \cdot 10^{-5}$ mol L^{-1} solution) using an ultrasound bath (Branson, model 1510, 42 kHz frequency) for 15 min. The solutions were maintained under stirring in the dark for 30 min, which allowed them to reach adsorption equilibrium and uniform dispersity, and we called the time zero the moment when the first aliquot was collected. The solutions were illuminated using six lamps (PHILIPS TL-D, 15 W each) in a photocatalytic system maintained at 20 °C in a thermostatic bath under stirring. After 5 min of irradiation, approximately 5 mL of each mixture was collected, and the catalysts were separated from the suspensions by centrifugation. Samples were collected every 5 min up to 60 min. The degradation process was monitored using UV–Vis absorption spectroscopy of the solutions using a V-660 spectrophotometer (JASCO). To determine the photodegradation mechanism of RhB, experiments were carried out following the same experimental procedure described previously. For these tests, 0.067 mg benzoquinone (BQ) (Alfa Aesar) was used to trap superoxide radicals ($O_2^{'}$), 0.088 g ammonium oxalate (AO) (Alfa Aesar) was used as hole scavenger, 0.0589 mL tert-butyl alcohol (TBA) (Alfa Aesar) was used to trap hydroxyl radicals (OH^*), and 0.1061 g AgNO$_3$ (Synth) was used as electron acceptor.

The structures of ZnO, C16MI.Cl, and ZnO/C1640 samples were analyzed using ATR-FTIR (Bruker Alpha-P, in the 4000–500 cm^{-1} range) as well as XPS. The XPS analysis was performed utilizing an Omicron-SPHERA station (Al Kα radiation, 1486.6 eV). The survey spectra were recorded with a 50 eV pass energy, and Cl 2p, N 1s, O 1s, and Zn 2p$_{3/2}$ regions were recorded with high resolution with pass energy of 20 eV.

Results and discussion

After obtaining the powders, polycrystallinity values of ZnO and ZnO/IL samples were evaluated using XRD patterns and Rietveld refinement analysis. Figure 2 shows the XRD patterns of the pure and modified ZnO samples.

The XRD patterns of ZnO, ZnO/C420, and ZnO/C1620 corresponded to the typical hexagonal wurtzite-type ZnO structure and were in agreement with the Inorganic Crystal Structure Database (ICSD) card no. 57450 for the pristine ZnO phase with P63mc space group. However, the ZnO/C440 and ZnO/C1640 composites showed quite different diffraction profiles, presenting also peaks at $2\theta = 11.3$ (003), 33.4 (202), 44.1 (119), and 58.2° (220). In order to better characterize the composites, we performed the Rietveld refinements for the XRD data of all samples. The obtained values for wt.% of each phase, lattice parameters, unit cell volumes, mean crystallite sizes ($<D_{X\text{-ray}}>$), isotropic strain, R weighted profile (R_{wp}) factors, and goodness-of-fit (S) values are presented in Table 2.

The data in Table 2 shows that, in addition to the ZnO phase, the presence of the trigonal simonkolleite Zn$_5$(OH)$_8$Cl$_2$H$_2$O structure (ICSD card no. 16973) was identified in the ZnO/C420, ZnO/C440, and ZnO/C1640 samples. Simonkolleite occurs as an oxidation product of Zn in the presence of the Cl$^-$ ions of the ILs. It might be inferred that the high concentration of Cl$^-$ ions led to the formation of the Zn$_5$(OH)$_8$Cl$_2$H$_2$O structure. However, the formation mechanism of simonkolleite is not clear and could consist of the following two main steps: (a) formation of the layered precipitate Zn (OH)$_2$ and (b) OH$^-$ groups being partially replaced by Cl$^-$ ions to form simonkolleite. The analysis data for the ZnO/C420 and ZnO/C440 composites indicated the formation of 6.41 and 15.02 wt.% of Zn$_5$(OH)$_8$Cl$_2$H$_2$O. However, only the
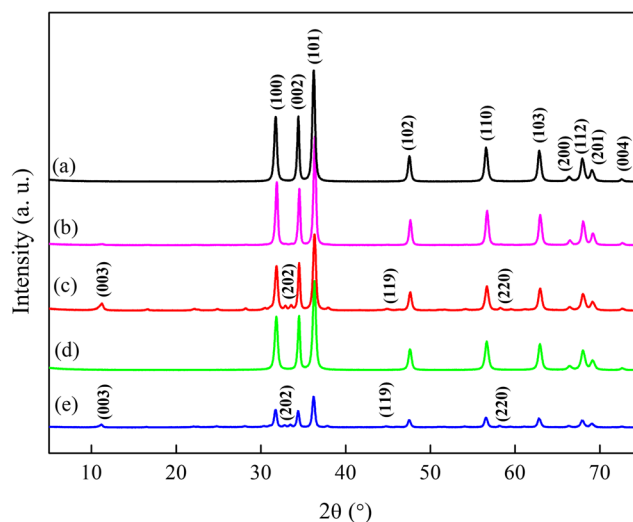

Fig. 2 XRD patterns of (**a**) ZnO, (**b**) ZnO/C420, (**c**) ZnO/C440, (**d**) ZnO/C1620, and (**e**) ZnO/C1640

Table 2 Rietveld refinement results of pure ZnO and prepared photocatalysts

Sample	Phase	Mass (%)	Lattice parameter $a = b$ (Å)	c (Å)	Cell volume V (Å^3)	$\langle D_{\text{X-ray}} \rangle$ (nm)	Strain (%)	R_{wp} (%)	S
ZnO	ZnO	100	3.25	5.21	47.68	171.7	0.296	5.47	1.51
ZnO/C420	ZnO	93.59	3.25	5.21	47.69	154.7	0.632	6.82	1.62
	Zn$_5$ (OH)$_8$Cl$_2$ (H$_2$O)	6.41	6.34	23.87	830.73	36.1	0.354		
ZnO/C440	ZnO	84.98	3.25	5.21	47.69	152.3	0.691	6.93	1.68
	Zn$_5$ (OH)$_8$Cl$_2$ (H$_2$O)	15.02	6.33	23.66	821.58	33.1	0.913		
ZnO/C1620	ZnO	100	3.25	5.21	47.69	130.7	0.317	5.59	1.49
ZnO/C1640	ZnO	82.69	3.25	5.21	47.69	126.9	0.461	6.26	1.14
	Zn$_5$ (OH)$_8$Cl$_2$ (H$_2$O)	17.31	6.34	23.65	823.3	36.2	0.373		

ZnO/C1640 sample indicated the formation of simonkolleite, while ZnO/C1620 did not. This can be explained by the presence of the higher alkyl chain of C16MI.Cl compared to BMI.Cl, which can prevent the chloride anions from approaching the ZnO particles, thus preventing the formation of simonkolleite. The simonkolleite phase of the ZnO/C420, ZnO/C440, and ZnO/C1640 samples presented lattice constants (a and c) of approximately 6.3 and 23.7 Å, respectively, and strong preferential orientation along the (003) plane, corresponding to a $2\theta_{(003)}$ angular position of approximately 11.1, which was attributed to its highly ordered reticular planes [32]. It can also be observed that, with the addition of ionic liquid, the mean crystallite size tends to decrease with increasing amount and size of the alkyl chain bound to the imidazole ring of the added IL. This behavior can be attributed to the fact that the stabilization of particles by the ionic liquid in aqueous medium can occur mainly by electrostatic and steric protection methods, preventing the formation of larger aggregates [33].

Figure 3 shows the Raman spectra of ZnO, ZnO/C420, ZnO/C440, ZnO/C1620, and ZnO/C1640 samples.

The Raman modes observed for pristine ZnO particles were 101, 203, 326, 381, 434, 569, and 661 cm^{-1}, which correspond to the active Raman modes of ZnO already reported in the literature [34, 35]. However, when IL was added to the ZnO samples, changes in the peak positions, line widths, and peak shapes of the Raman modes can be observed. These changes could be attributed to the non-homogeneity of the particle size distribution, defects, and non-stoichiometry of the samples. Rietveld refinement data showed that the ZnO/C420, ZnO/C440, and ZnO/C1640 samples presented the simonkolleite phase; however, their spectra did not exhibit Raman modes attributed to this compound [32]. The Raman modes of 238, 242, 269, and 393 cm^{-1} of the simonkolleite phase may not have been observed because they were close to the pure ZnO modes, and the incorporation of the ILs into ZnO caused the peaks to widen and shift, causing the Raman modes of ZnO and simonkolleite to overlap.

Pure ZnO, ZnO/C440, and ZnO/C1640 were characterized using N$_2$ adsorption-desorption isotherms. According to the IUPAC, the isotherms of all samples (Fig. 4) can be categorized as type IV, with distinct hysteresis loops, which confirmed the presence of mesoporous materials.

Incorporating ILs into ZnO particles resulted in a decrease in the surface area of the prepared ZnO/C440 (8.3 m^2 g^{-1}) catalyst compared to pure ZnO (13.0 m^2 g^{-1}). However, the prepared ZnO/C1640 catalyst exhibited an increase in surface area (17.3 m^2 g^{-1}) compared to the other samples. The mean pore diameters of the ZnO, ZnO/C440, and ZnO/C1640 samples were 15.3, 13.0, and 14.0 nm, respectively, which, considering the experimental errors, are not significantly different. In addition, pore volume followed the same trend as surface area, decreasing from 0.060 to 0.029 cm^3 g^{-1} for pure ZnO and ZnO/C440 and increasing for ZnO/C1640 to 0.064 cm^3 g^{-1}. The mean diameter of the crystallites is inversely proportional to specific surface area, i.e., the larger the specific surface area, the smaller the diameter [36]. The ZnO/C440 and ZnO/C1640 samples had mean crystallite sizes of 152.3 and 126.9 nm and specific areas of 8.3 and 17.3 m^2 g^{-1}, respectively, indicating that the obtained data follows this trend. This increase in specific surface area could be attributed to the IL of the ZnO/C1640 catalyst (C16MI.Cl) being possibly adsorbed by the ZnO particles and stabilizing these particles in smaller sizes, while the IL of the ZnO/C440 catalyst (BMI.Cl) could have entered the ZnO structure, causing this particle to increase its diameter. In addition, we observed in the DRX results that this sample presents a secondary phase (Zn$_5$(OH)$_8$Cl$_2$·(H$_2$O)) which has a higher cell volume, which in turn reflects in increased particle size.

Figure 5 shows FEG-SEM images of ZnO, ZnO/C420, ZnO/C440, ZnO/C1620, and ZnO/C1640.

It can be observed in Fig. 5(a) that ZnO presents flower-like shape in its morphology. These structures are assembled by a large number of nanosheets that intersect with each other, resulting in a net-like structure with porous surfaces. When ILs were added to ZnO (Fig. 5(c–e)), the morphology of the ZnO particles remained the same. TEM results indicate that the presence of IL does not exert any major influence in the crystal structure of ZnO (Fig. S1). The resulting histograms show that the tendency of the particles is to decrease with

Fig. 3 Raman spectra of (**a**) ZnO, ZnO/C420, and ZnO/C440 and (**b**) ZnO, ZnO/C1620, and ZnO/C1640

Fig. 4 N_2 adsorption-desorption isotherms of ZnO, ZnO/C440, and ZnO/C1640
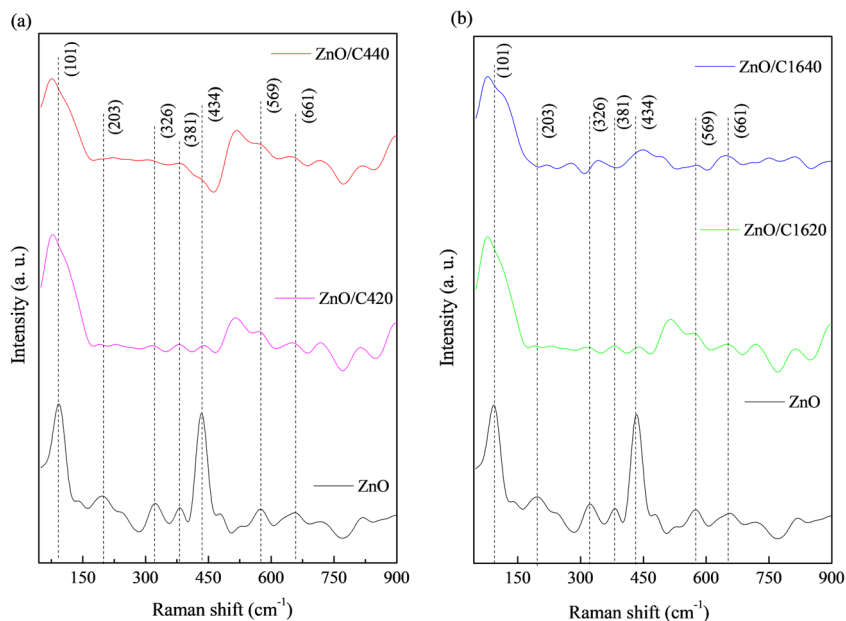
increased ionic liquid concentration. However, the mean diameter (Av) of ZnO particles increases from 1.14 to 1.79 μm with the addition of 20 wt.% BMI.Cl and standard deviation (SD) changing from 0.26 to 0.32 μm. This behavior can be attributed to a higher cell volume of the secondary phase ($Zn_5(OH)_8Cl_2(H_2O)$) which reflects in an increase in particle size. Nevertheless, the addition of 40 wt.% BMI.Cl IL stabilizes the ZnO particles in smaller sizes, with mean diameter of 0.92 μm and standard deviation of 0.32 μm. In addition, the introduction of C16MI.Cl stabilizes the oxide particles in small and uniform diameters, with mean of 0.82 and 0.78 μm and SD of 0.15 and 0.32 μm for ZnO/C1620 and ZnO/C1640, respectively. The data indicates that the IL may be surrounding the surface of the particle and can enter the structure depending on the size of its cation. Therefore, the

chemical and physical interactions between IL and ZnO particles play an important role in determining the structure of the particles, with the diameter being dependent on the amount of ionic liquid added and the size of the cation.

UV–Vis spectroscopic measurements were performed to investigate the effect of adding BMI.Cl and C16MI.Cl on the optical properties of pristine ZnO. From the UV–Vis data, the band gap energies (E_g, in eV) of the samples were calculated using the Kubelka-Munk's method [37] described by the following equation:

$$\alpha h\nu = A\left(h\nu - E_g\right)^n$$

where α is the linear absorption coefficient of the material, $h\nu$ is the incident photon energy, A is a proportionality constant related to the material, and n is a constant associated with different types of electronic transitions. As previously reported, ZnO is an n-type direct band gap semiconductor with $n = 1/2$ [38]. The E_g values of all the analyzed samples are shown in Fig. 6.

The E_g values of ZnO, ZnO/C420, ZnO/C440, ZnO/C1620, and ZnO/C1640 were 3.20, 3.14, 3.09, 3.13, and 2.26 eV, respectively. The values of ZnO, ZnO/C420, and ZnO/C1620 were very similar; however, the values of ZnO/C440 and ZnO/C1640 were lower compared to the other samples. This reduction in E_g values can be attributed to the fact that these samples presented higher mass percentages of $Zn_5(OH)_8Cl_2H_2O$. Simonkolleite is a wide band gap semiconductor with electronic band structure similar to that of ZnO (E_g of 3.3 eV) [39]. These results indicate that the exponential optical absorption edge and the optical band gap energy are controlled by the degree of structural disorder in the lattice. In the ZnO/C1640 sample, we observed a small E_g value
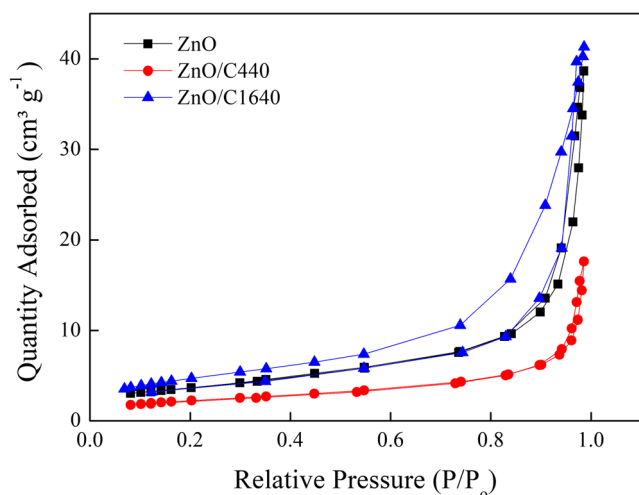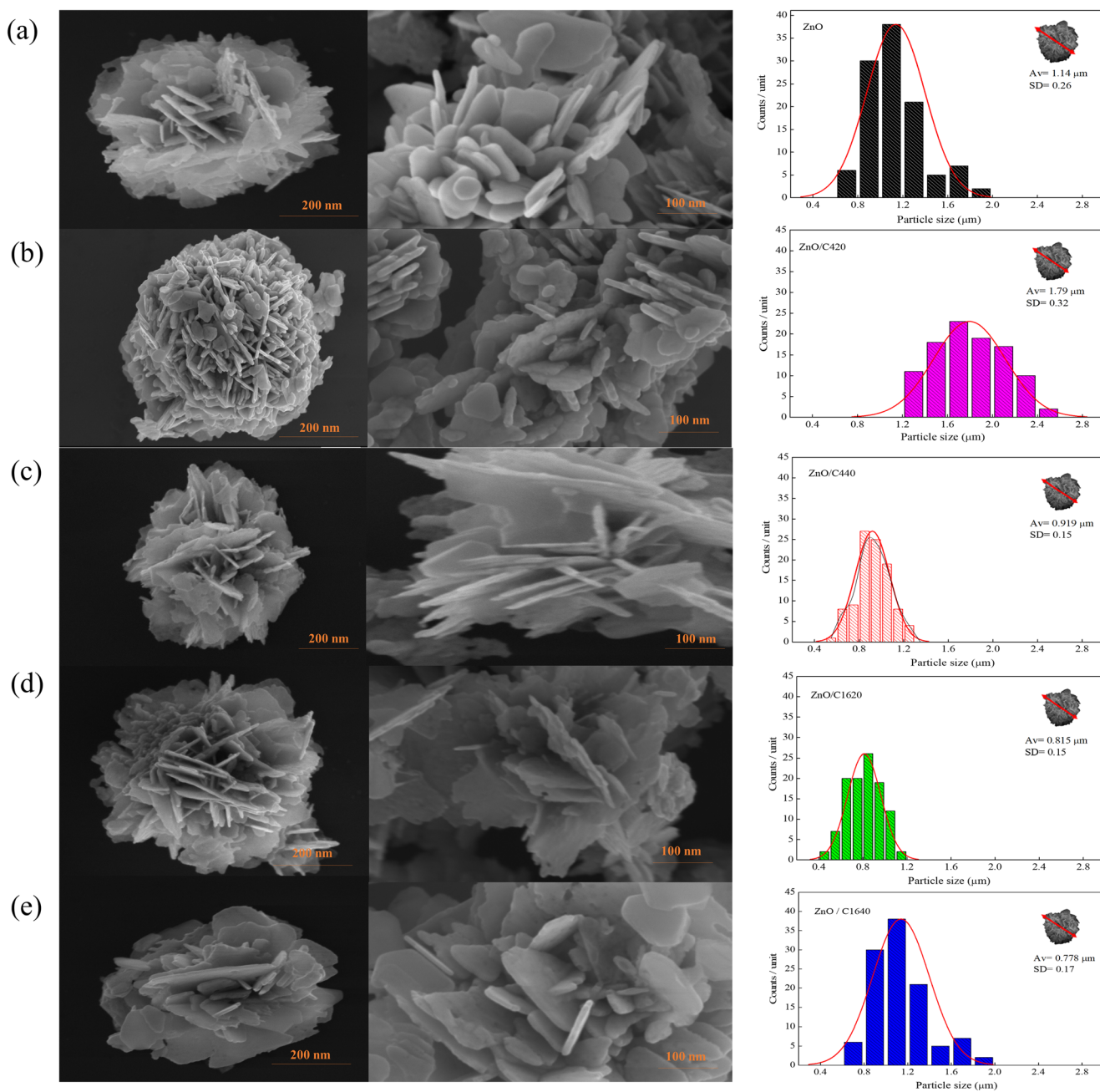
Fig. 5 FEG-SEM micrographs and size distributions of (**a**) ZnO, (**b**) ZnO/C420, (**c**) ZnO/C440, (**d**) ZnO/C1620, and (**e**) ZnO/C1640

accompanied by a greater slope of the curve. This behavior indicates that the IL causes the formation of defects or local distortion in the ZnO structure, which provokes redistribution in the density of states and introduces intermediate electronic defect states in the band gap. Normally, these energy states originated from the formation of oxygen vacancies in the structure, as a consequence of a symmetry break between the (lattice former)-O and (lattice modifier)-O bonds [40, 41]. The decrease in E_g value could be also explained by the deeper defects created in the samples by adding ILs to ZnO. Therefore, adding simonkolleite reduced the E_g value and could also enhance the activity of ZnO under visible light.

Figure 7 shows the PL spectra and deconvolution of the three peaks for ZnO, ZnO/C420, ZnO/C440, ZnO/C1620, and ZnO/C1640 using an excitation laser with $\lambda = 350$ nm at 25 °C.

The PL spectrum of pristine ZnO presented a broad band with the emission maximum centered at 2.0 eV ($\lambda = 619.1$ nm). When BMI.Cl and C16MI.Cl were added to ZnO particles, the emission maxima are shifted to 1.86 eV ($\lambda = 666.6$ nm) for both ILs at all concentrations. In order to verify the changes in PL properties and contributions of each individual peak caused by the addition of IL in the ZnO particles, deconvolution was performed using the PickFit
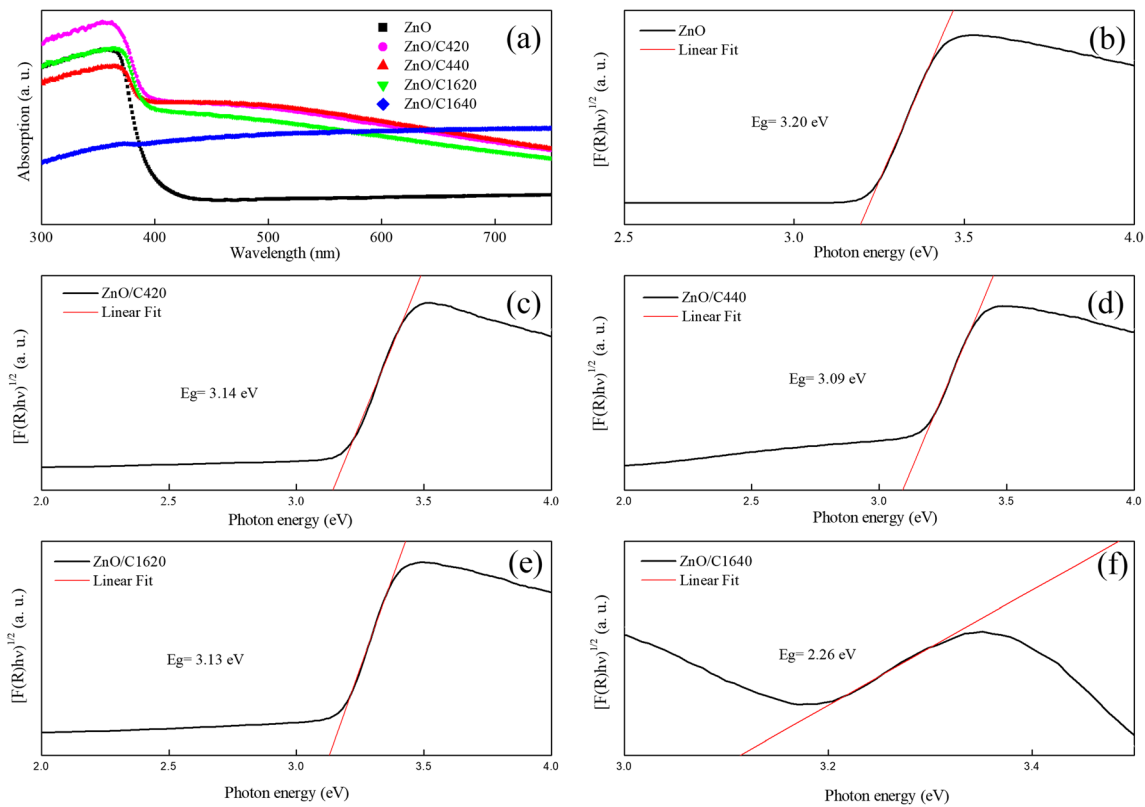
Fig. 6 (a) UV–Vis absorbance spectra, (b–f) E_g values of ZnO, ZnO/C420, ZnO/C440, ZnO/C1620, and ZnO/C1640, respectively

software with Voigt area function (Fig. 7(b–f)). The spectrum of pristine ZnO had three components with energies centered at 2.22, 1.97, and 1.78 eV, to which the colors green, orange, and red were attributed, respectively (Fig. 7(b)). Deconvolution analysis showed a higher contribution percentage in the green region (43.1%), which could be related to shallow defects. These defects could be attributed to recombination of isolated electrons in the vacancies of ionized oxygen (V_0) with photo-generated holes [42]. The spectra of ZnO/C420, ZnO/C440, ZnO/C1620, and ZnO/C1640 showed the contribution of the three components located at the same energy values as those of ZnO particles (Fig. 7(c–f)). The deconvolutions of these spectra showed shifts of their emission maxima to the left (red region), accompanied by decreasing contributions in the green regions. However, for the ZnO/C1640 sample, the percentage of orange color was equal to that of pristine ZnO and the percentage of green color increases with IL concentration. These changes in contributions could be explained by the presence of ILs in ZnO decreasing the density of shallow defects and increasing the density of deeper defects. The deeper defects in the ZnO/C420, ZnO/C440, and ZnO/C1640 samples might be attributed to the presence of displacements or precipitates in the samples [43]. These displacements could be caused by the increase in the number of oxygen vacancies, since simonkolleite formed in these samples. Like ZnO, simonkolleite is electrically and chemically active due to the presence of these oxygen vacancies on its surface. These vacancies may function as n-type donors

and, thus, significantly increase the conductivity of the material [44].

The photocatalytic degradation performance of RhB dye was analyzed in order to investigate the photocatalytic activity of ZnO, C16MI.Cl, ZnO/C420, ZnO/C440, ZnO/C1620, and ZnO/C1640 (Fig. 8).

Figure 8(a–f) shows the UV–Vis spectra of the degraded RhB after photocatalytic degradation under visible light. For all samples, the degraded dye exhibited maximum absorption at 554 nm wavelength. The relative intensity values at the maximum absorption wavelength decreased for ZnO particles and C16MI.Cl IL, reaching 0.81 and 1.07, respectively, after 60 min. However, when 20 and 40 wt.% BMI.Cl were incorporated to pristine ZnO, the relative intensity values at the maximum absorption wavelength decreased to 0.7 and 0.6, respectively. When the same weight percentages of C16MI.Cl were incorporated into ZnO particles, the relative intensities of the maximum absorption wavelengths decreased to 0.6 and 0.4, respectively. These results are evidence of the influence of the alkyl chain size and simonkolleite phase on dye degradation rate.

Figure 8(g) shows the C/C_0 vs. time plot for RhB dye degradation. Adding pure IL did not cause the dye to degrade; however, when pure ZnO was added, a small degree of degradation was observed, and equilibrium was reached after 45 min. When the composite samples were tested, similar degradation performance was observed for the ZnO/C420
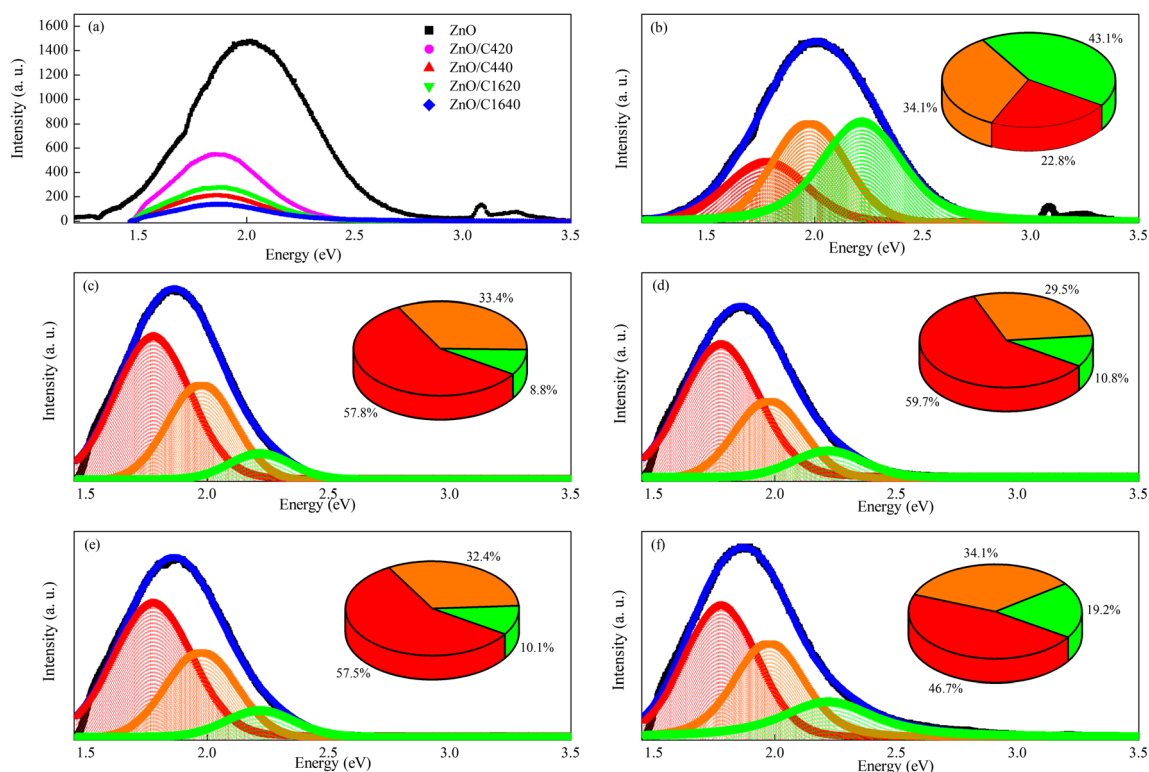
Fig. 7 (**a**) Comparison of intensities of PL curves for all samples, (**b**–**f**) PL curves and deconvolution of three peaks of ZnO, ZnO/C420, ZnO/C440, ZnO/C1620, and ZnO/C1640, respectively

and ZnO/C1620 samples. However, when the amount of IL was increased to 40 wt.%, the ZnO/C1640 sample presented a better performance for dye degradation under visible light.

The degradation of RhB when C16MI.Cl, ZnO, ZnO/ C420, ZnO/C440, ZnO/C1620, and ZnO/C1640 were used was 4, 30, 40, 47, 42, and 62%, respectively, during the same time interval (Fig. 8(h), Table 3). These results demonstrate that the addition of IL enhanced the efficiency of pristine ZnO for dye degradation. Furthermore, an increase in degradation rate was observed with the increase in the length of the alkyl chain of the IL. As can be observed from the Rietveld results (Table 2), the ZnO/ C440 and ZnO/C1640 composites contained simonkolleite phases in their structures. This can be correlated to the increase in the efficiency of degradation observed for these samples. Moreover, as the IL concentration increased, the concentration of the simonkolleite complex also increased. The ZnO/C1640 sample exhibited the best photodegradation performance of all samples. These results demonstrate that the formation of simonkolleite, the higher surface area (Fig. 4), and size of the alkyl chains attached to the imidazolium ring exerted strong influence on the performance of the catalyst.

Figure 8(i) shows a − ln C_n/C_0 vs. time plot, and Table 3 shows values obtained for the rate constant, for all samples. Since the photodegradation behavior of RhB dye can be

considered a pseudo-first-order reaction, this constant can be obtained when the degradation curve was fitted in the following equation:

$$\ln \left({}^{C_0}/_C \right) = -kt$$

where k is the rate constant (min^{-1}) and C_0 and C are the RhB dye concentration values at times 0 and t, respectively.

The ZnO/C1640 sample exhibited the highest photocatalytic activity of all samples, with $k = 0.00954$ min^{-1}. This value was approximately 1.9 times greater than that of pure ZnO (0.00501 min^{-1}) and 23 times greater than that of C16MI.Cl (0.000414 min^{-1}). The increase in the value of k could be attributed to a decrease in the probability of recombination of the electron/hole pairs, which could lead to an increase in the number of electron donors of the ZnO/C1640 sample, causing its photocatalytic activity to increase [45].

The cluster-like elucidation of photocatalyst performance was supported by different bulk (intrinsic) and superficial (extrinsic) defect distributions, inducing material property changes in symmetry in the short, medium, and long ranges. The ordered complex cluster often behaved as an electron sink and improved charge separation within the semiconductor. The electron polarons could be discharged from the ordered complex cluster to disordered complex clusters. Effective charge separation (electron/ hole) was considered in terms of $[ZnO_4]_o^x$ and $[ZnO_3V_o^x$
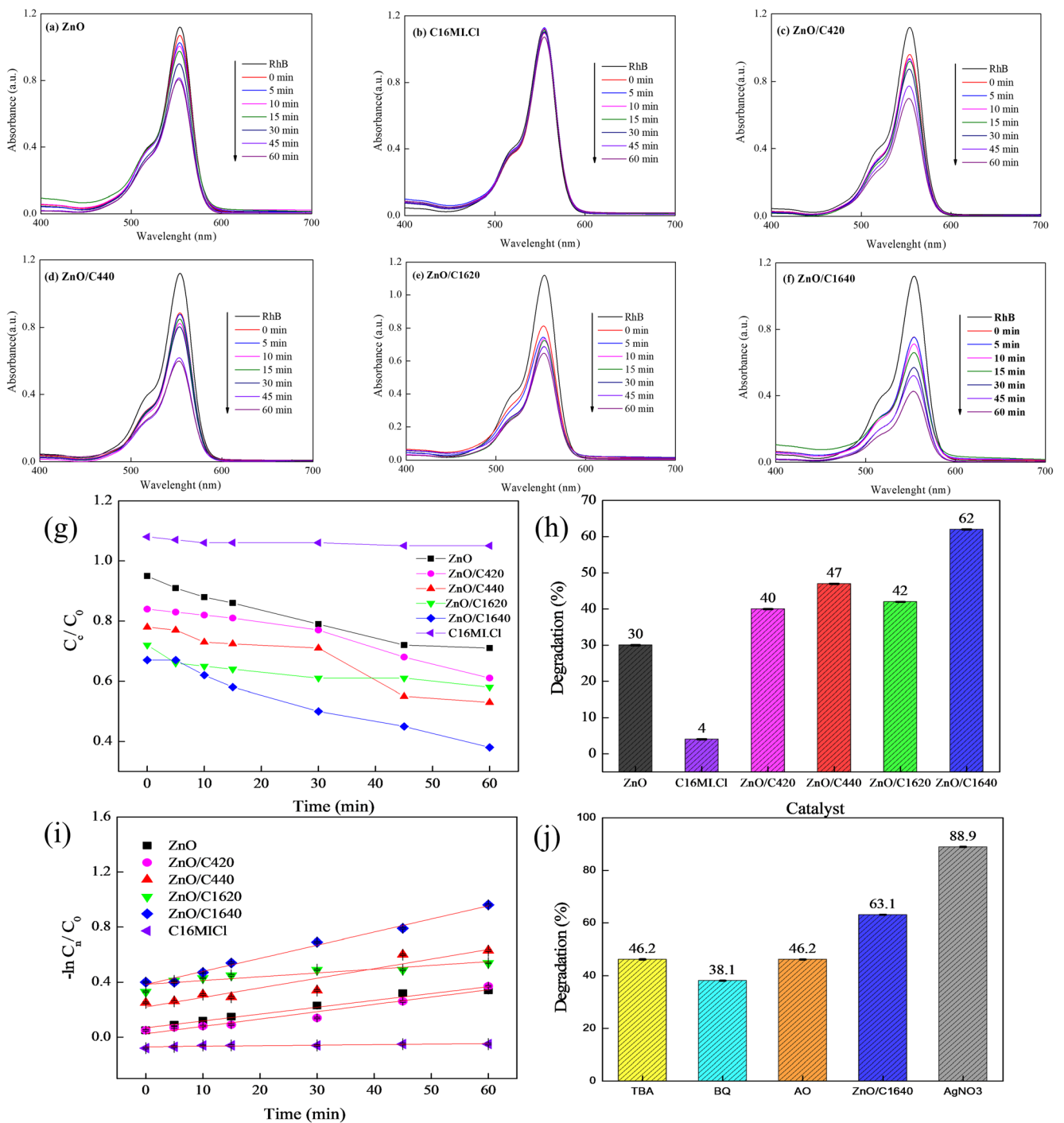
Fig. 8 Photocatalytic performance of ZnO, C16MI.Cl, ZnO/C420, ZnO/C440, ZnO/C1620, and ZnO/C1640 for RhB degradation

]$_d$ complex clusters, where o is order and d is disorder. The intrinsic and extrinsic effects when a hole is in an acceptor state and an electron in a donor state can be expressed using the following equation, where Kröger-Vink notations were used for complex clusters [46]:

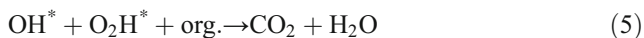$$[ZnO_4]_o^x + [ZnO_3V_o^x]_d \rightarrow [ZnO_4]_o' + [ZnO_3V_o']_d$$
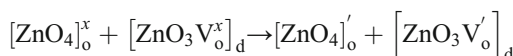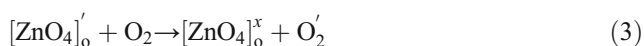
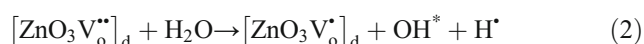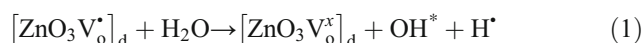According to the literature, the main factor responsible for the high-efficiency photocatalysis of the catalyst crystals is the low recombination rate between photogenerated electrons (′) and holes (•) on the surface of semiconductors. Our ZnO semiconductor catalyst already had the ability to generate ′ ↔ • pairs. This characteristic was due to the intrinsic defects in the lattice of the semiconductor materials with intermediate

Table 3 Degradation data and the rate constant (k) values of C16MI.Cl, ZnO, ZnO/C420, ZnO/C440, ZnO/C1620, and ZnO/C1640

Sample	Degradation (%)	k (min^{-1})
ZnO	30	0.00501
C16MI.Cl	4	0.000414
ZnO/C420	40	0.00523
ZnO/C440	47	0.00689
ZnO/C1620	42	0.00276
ZnO/C1640	62	0.00954

levels in the forbidden region of the valence band with the conduction band. Therefore, each defect on the surface of semiconductors acted as a catalytic active site due to the different surface energy values, as shown in Fig. 8. During the photo-oxidation processes, the reducing clusters interacted with water molecules, producing hydroxyl radicals and hydrogen. On the other hand, the oxidant clusters yielded electrons to oxygen (O_2'), as shown in Fig. 8 and Eqs. (1)–(5):

$$\left[ZnO_3V_o^\bullet\right]_d + H_2O \rightarrow \left[ZnO_3V_o^x\right]_d + OH^* + H^\bullet \tag{1}$$

$$\left[ZnO_3V_o^{\bullet\bullet}\right]_d + H_2O \rightarrow \left[ZnO_3V_o^\bullet\right]_d + OH^* + H^\bullet \tag{2}$$

$$\left[ZnO_4\right]_o' + O_2 \rightarrow \left[ZnO_4\right]_o^x + O_2' \tag{3}$$

$$O_2' + H^\bullet \rightarrow O_2H^* \tag{4}$$

$$OH^* + O_2H^* + org. \rightarrow CO_2 + H_2O \tag{5}$$

In order to study the RhB photodegradation mechanism, experiments were carried out following the same experimental procedure previously used and the ZnO/C1640 sample which presented the best results in the previous experiments, but adding the following scavengers: hydroxyl radicals (OH*), holes ($^\bullet$), superoxide radicals (O_2'), and an electron acceptor. For all tests, each scavenger was added separately to the mixture of dye and ZnO/C1640 sample. Figure 8(j) shows the results of the photocatalytic activity tests, which were performed in order to propose a photocatalytic mechanism. The results show that the removal rates of RhB when BQ, TBA, and AO were added decreased to 38, 46, and 46%, respectively. On the other hand, the enhancement in photodegradation rate when AgNO$_3$ was added could be attributed to the silver ions acting as electron acceptors in order to reduce the recombination rate of the photogenerated electron/hole pairs [47]. Therefore, the superoxide radical (O_2') can be the main reactive species during the photocatalytic degradation of RhB dye, as it caused a decrease of approximately 25% in the degradation rate.

The obtained results showed that the formation of simonkolleite when the IL was added increased the performance of ZnO in the photodegradation of RhB dye.

Simonkolleite is recognized as a wide band gap semiconductor presenting an electronic band structure similar to that of ZnO [48], thus having the ability to decompose organic dyes [39]. The enhancement in photocatalytic activity of the samples containing $Zn_5(OH)_8Cl_2H_2O$ phases can be ascribed to the Zn^{2+} ions, which helped to inhibit the electron/hole pair recombination and enhanced the interfacial charge transfer reactions [49]. Badawy et al. [32] improved the electrochemical/photochemical properties of TiO$_2$ by adding 10% simonkolleite. They observed that the simonkolleite/TiO$_2$ sample presented a higher photocatalytic activity than the pure TiO$_2$ nanoparticles. Remazole Brilliant Red F3B dye was degraded in 41.5 min using simonkolleite/TiO$_2$ and 58.3 min using TiO$_2$.

Although XRD data had shown that, while the ZnO/C1620 sample did not present the formation of the $Zn_5(OH)_8Cl_2H_2O$ phase, its performance in the photodegradation of RhB dye was similar to that of the ZnO/C420 sample. This non-complex formation can be explained by the BET results, which showed that ZnO/C1640 presented a larger surface area (17.3 m^2 g^{-1}), which may mean that C16MI.Cl had surrounded the ZnO structure due to its large alkyl chain. This behavior can explain why no simonkolleite complex formed when only 20 wt.% C16MI.Cl was added, since a larger amount (40 wt.%) of the long-alkyl chains was closer to the ZnO structure, facilitating the oxidation of zinc. This behavior was not observed for BMI.Cl because it has a shorter alkyl chain than that of C16MI.Cl; therefore, it could enter the pores of ZnO, as can be observed from the decrease in surface area from the BET data.

In order to obtain evidence of the interaction between ZnO particles and C16MI.Cl IL during the formation of the $Zn_5(OH)_8Cl_2H_2O$ phase, FTIR and XPS analyses were performed. The FTIR results are shown in Fig. 9.
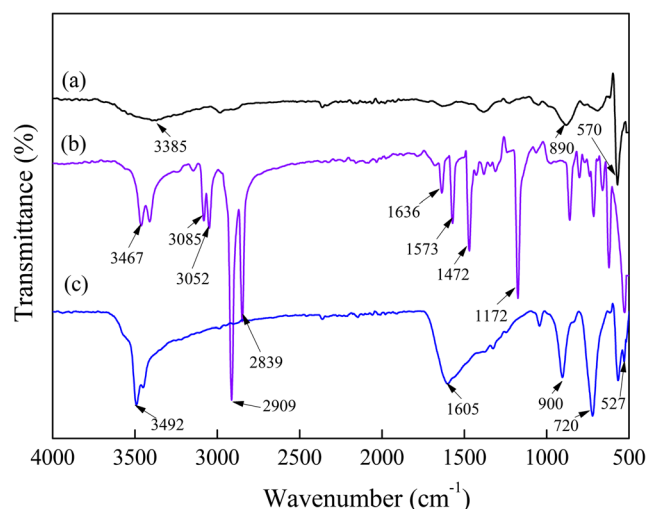
Fig. 9 ATR-FTIR spectra of (**a**) ZnO, (**b**) C16MI.Cl, and (**c**) ZnO/C1640

The FTIR spectrum of ZnO shows a broad peak centered at 3385 cm^{-1} attributed to O–H stretching. The peaks at 960 and 570 cm^{-1} are the characteristic absorption peaks of the stretching of Zn–O bonds [50]. On the other hand, pure C16MI.Cl spectrum displays peaks at 1172 and 1472 cm^{-1} arising from the in-plane ring C–H deformation and the CH$_3$C–H deformation, respectively. The peaks at 1573 and 1636 cm^{-1} are related to the stretching of the C=N and C=C rings, respectively. The peaks at 2839 and 2909 cm^{-1} were assigned to the aliphatic C–H stretch. The absorption peaks at 3052 and 3085 cm^{-1} were attributed to the ring C–H stretch. The peak at 3467 cm^{-1} could be attributed to the O–H stretch from the absorbed water in the sample [51]. However, ZnO/ C1640 showed a different spectrum than the rest of the pure samples. The broad peak at 1605 cm^{-1} can be assigned to the deformation vibration of H$_2$O molecules. The characteristic O–H stretching vibration is found at 3492 cm^{-1}; the strong

peaks at 900 and 720 cm^{-1} were due to the stretching vibration modes of the Cl$^-$ ion [52]; and the peak at 527 cm^{-1} is related to the Zn–O bond [53]. These FTIR data were in agreement with the XRD patterns and had confirmed that simonkolleite typically formed when high concentrations of C16MI.Cl were used.

We carried out XPS measurements in order to obtain more detailed information about the elemental compositions and chemical states of ZnO and ZnO/C1640 samples, and the results are presented in Fig. 10.

Figure 10(a) shows the survey spectra of ZnO and ZnO/ C1640 particles where only the elemental peaks of Zn, O, and C are present. The presence of C in both samples could be attributed to the XPS instrument. Additional Cl (Fig. 10(b)) and N (Fig. 10(c)) peaks were observed for the ZnO/C1640 sample; these elements are found in C16MI.Cl IL. Figure 10(d) shows the comparison of the asymmetric O 1s
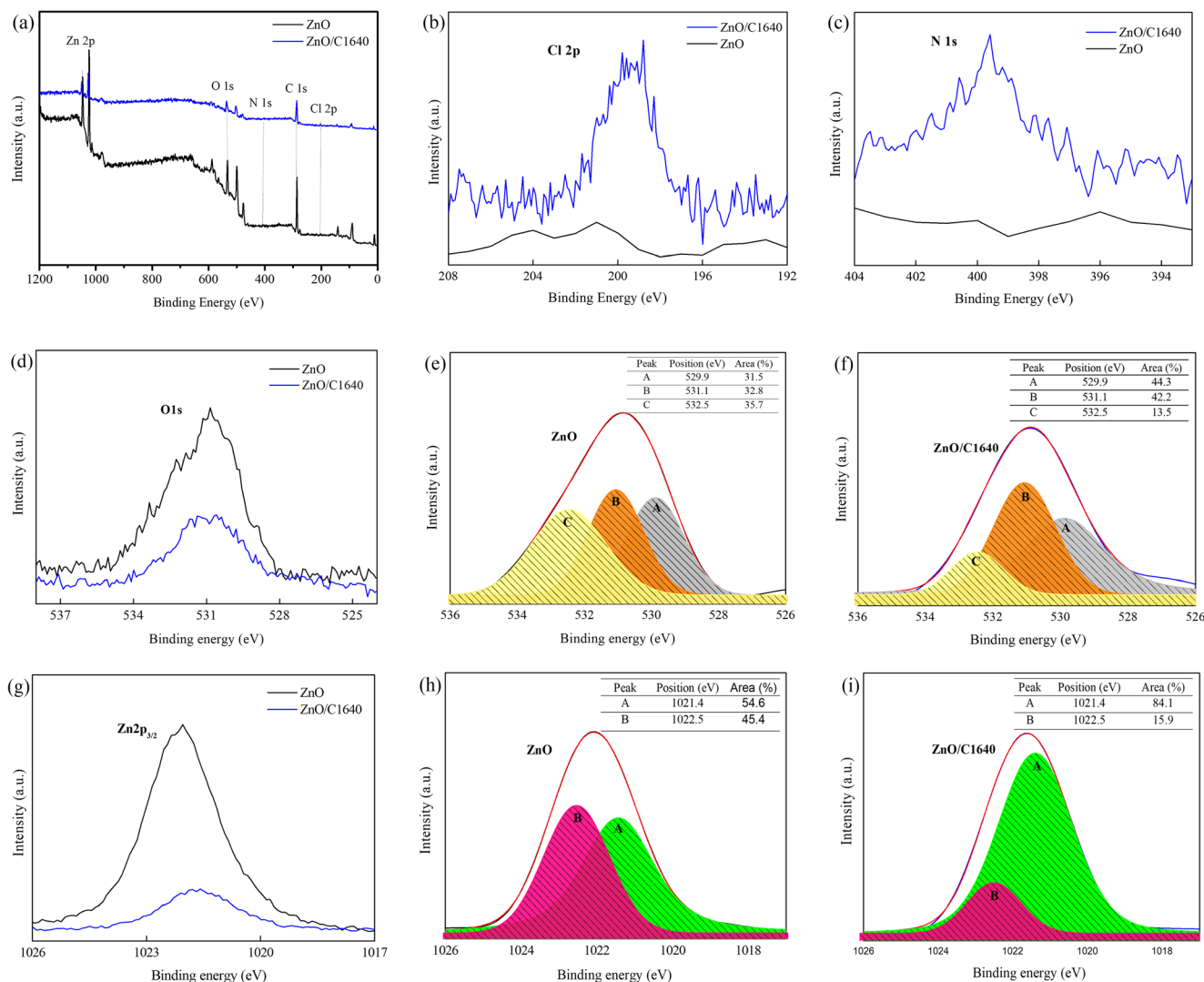

Fig. 10 XPS spectra of ZnO and ZnO/C1640 samples: (**a**) survey spectrum, (**b**) Cl 2p, (**c**) N 1s, (**d**) O 1s, (**e**) deconvolution of the two O 1s peaks of ZnO, (**f**) deconvolution of the two O 1s peaks of ZnO/C1645, (**g**) Zn 2p$_{3/2}$, (**h**) deconvolution of the two Zn 2p$_{3/2}$ peaks of ZnO, and (**i**) deconvolution of the two Zn 2p$_{3/2}$ peaks of ZnO/C1640

peaks of the samples and Fig. 10(e, f) shows the three Gaussian curves (A, B, and C) of ZnO and ZnO/C1645 samples. Peak A, centered at 529.9 eV, could be associated with the O^{2-} ion of the ZnO wurtzite structure surrounded by Zn atoms with their full complement of the nearest-neighbor O^{2-} ions. Peak B, centered at 531.1 eV, could be ascribed to the presence of OH bonds. Finally, peak C, centered at 532.5 eV, could be attributed to the surface-adsorbed species, such as CO_2, H_2O, or O_2 [54, 55]. It can be observed that the insertion of the IL into the ZnO particles caused a reduction in the area of peak C and increased the areas of A and B peaks. The approximately 9.5% increase in the area of the B peak could be attributed to the increase in the amount of OH bonds at the surface. As a result of this increase in the amount of hydroxyl radicals, the ZnO/C1640 sample presented a superior performance during the photodegradation of RhB when compared to the other analyzed samples. The resolution Zn $2p_{3/2}$ spectrum in Fig. 10(g) indicates the presence of Zn^{2+} ions in the ZnO wurtzite structure of both samples [56]. In order to estimate the evolution of the Zn^{2+}/Zn^0 ratio, two Gaussian curves were applied to the Zn$2p_{3/2}$ spectra. The contributions centered at 1021.4 and 1022.5 eV (peaks A and B) were associated with Zn^0 and Zn^{2+}, respectively. Figure 10(h), i shows that the impregnation of the IL into the ZnO particles caused a significant reduction in the number of Zn^{+2} ions and an increase in the number of Zn^0 particles of approximately 29.5%. This behavior could indicate that interstitial zinc may have formed due to the bombardment by energetic O^{2-} ions [57]. Based on these results, we concluded that the ZnO/C1640 sample could be used for the photocatalytic degradation of RhB dye under visible light and that it could exhibit a better performance than pure ZnO.

Conclusions

ZnO particles synthesized using the MAH method were incorporated with BIM.Cl or C16MI.Cl ILs and analyzed for photocatalytic degradation of RhB dye. XRD analysis, FEG-SEM, and PL measurements were used in order to confirm the formation of the ZnO/IL composites and of the $Zn_5(OH)_8Cl_2H_2O$ phase in the ZnO/C420, ZnO/C440, and ZnO/C1640 samples. The photocatalytic performance revealed that RhB dye degradation reached 62% for the ZnO/C1640 sample and only 30% for the pure ZnO sample, at the same time interval. This improvement in photocatalytic performance could be attributed to the formation of simonkolleite and the size of the alkyl chain attached to the imidazolium ring of the ILs, since the results showed that these chains exerted strong influence on the performance of the catalyst.

References

1. Peter CN, Anku WW, Sharma R, Joshi GM, Shukla SK, Govender PP (2018) N-doped ZnO/graphene oxide: a photostable photocatalyst for improved mineralization and photodegradation of organic dye under visible light. Ionics. https://doi.org/10.1007/s11581-018-2571-x
2. Baldez EE, Robaina NF, Cassella RJ (2008) Employment of polyurethane foam for the adsorption of methylene blue in aqueous medium. J Hazard Mater 159:580–586. https://doi.org/10.1016/j.jhazmat.2008.02.055
3. Nagaraja R, Kottam N, Girija CR, Nagabhushana BM (2012) Photocatalytic degradation of rhodamine B dye under UV/solar light using ZnO nanopowder synthesized by solution combustion route. Powder Technol 215-216:91–97. https://doi.org/10.1016/j.powtec.2011.09.014
4. Chen CC, Liu P, Lu CH (2008) Synthesis and characterization of nano-sized ZnO powders by direct precipitation method. Chem Eng J 144:509–513. https://doi.org/10.1016/j.cej.2008.07.047
5. Khayyat AS, Akhta MS, Umar A (2012) ZnO nanocapsules for photocatalytic degradation of thionine. Mater Lett 81:239–241. https://doi.org/10.1016/j.matlet.2012.04.039
6. Gupta VK, Jain R, Mittal A, Saleh TA, Nayak A, Agarwal S, Sikarwar S (2012) Photo-catalytic degradation of toxic dye amaranth on TiO2/UV in aqueous suspensions. Mater Sci Eng C 32:12–17. https://doi.org/10.1016/j.msec.2011.08.018
7. Cao S, Low J, Yu J, Jaroniec M (2015) Polymeric photocatalysts based on graphitic carbon nitride. Adv Mater 27:2150–2176. https://doi.org/10.1002/adma.201500033
8. Zhou H, Qu Y, Zeid T, Duan X (2012) Towards highly efficient photocatalysts using semiconductor nanoarchitectures. Energy Environ Sci 5:6732–6743. https://doi.org/10.1039/C2EE03447F
9. Elango G, Roopan SM (2016) Efficacy of SnO2 nanoparticles toward photocatalytic degradation of methylene blue dye. J Photochem Photobiol B 155:34–38. https://doi.org/10.1016/j.jphotobiol.2015.12.010
10. Basahel SN, Ali TT, Mokhtar M, Narasimharao K (2015) Influence of crystal structure of nanosized ZrO2 on photocatalytic degradation of methyl orange. Nanoscale Res Lett 10:73–78. https://doi.org/10.1186/s11671-015-0780-z
11. Repo E, Rengaraj S, Pulkka S, Castangnoli E, Suihkonen S, Sopanen M, Sillanpää M (2013) Photocatalytic degradation of dyes by CdS microspheres under near UV and blue LED radiation. Sep Purif Technol 120:206–214. https://doi.org/10.1016/j.seppur.2013.10.008
12. La Porta FA, Nogueira AE, Gracia L, Pereira WS, Botelho G, Mulinari TA, Andrés J, Longo E (2017) An experimental and theoretical investigation on the optical and photocatalytic properties of ZnS nanoparticles. J Phys Chem Solids 103:179–189. https://doi.org/10.1016/j.jpcs.2016.12.025
13. Konstantinou IK, Albanis TA (2004) TiO2-assisted photocatalytic degradation of azo dyes in aqueous solution: kinetic and mechanistic investigations: a review. Appl Catal B Environ 49:1–14. https://doi.org/10.1016/j.apcatb.2003.11.010
14. Balcha A, Yadav OP, Dey T (2016) Photocatalytic degradation of methylene blue dye by zinc oxide nanoparticles obtained from precipitation and sol-gel methods. Environ Sci Pollut Res Int 23:25485–25493. https://doi.org/10.1007/s11356-016-7750-6
15. Ma S, Xue J, Zhou Y, Zhang Z (2014) Photochemical synthesis of ZnO/Ag2O heterostructures with enhanced ultraviolet and visible

photocatalytic activity. J Mater Chem A 2:7272–7280. https://doi.org/10.1039/C4TA00464G

16. Ghosh A, Guha P, Samantara AK, Jena BK, Bar R, Ray SK, Satyam PV (2015) Simple growth of faceted Au–ZnO hetero-nanostructures on silicon substrates (nanowires and triangular nanoflakes): a shape and defect driven enhanced photocatalytic performance under visible light. ACS Appl Mater Interfaces 7(18):9486–9496. https://doi.org/10.1021/acsami.5b00634

17. Sadeghia R, Karimi-Malehb H, Baharic A, Taghavi M (2013) A novel biosensor based on ZnO nanoparticle/1,3-dipropylimidazolium bromide ionic liquid-modified carbon paste electrode for square-wave voltammetric determination of epinephrine. Phys Chem Liq 51:704–714. https://doi.org/10.1080/00319104.2013.782547

18. Zsilák Z, Szabó-Bárdos E, Fónagy O, Horváth O, Horváth K, Hajós P (2014) Degradation of benzenesulfonate by heterogeneous photocatalysis combined with ozonation. Catal Today 230:55–60. https://doi.org/10.1016/j.cattod.2013.10.039

19. Carvalho RG, Tavares MTS, Oliveira FKF, Nascimento RM, Longo E, Li MS, Paskocimas CA, Bomio MRD, Motta FV (2017) Preparation and photocatalytic properties of hexagonal-shaped ZnO:Sm^{3+} by microwave-assisted hydrothermal method. J Mater Sci Mater Electron 28:7943–7950. https://doi.org/10.1007/s10854-017-6496-3

20. Sin JC, Lam SM (2016) Hydrothermal synthesis of europium-doped flower-like ZnO hierarchical structures with enhanced sunlight photocatalytic degradation of phenol. Mater Lett 182:223–226. https://doi.org/10.1016/j.matlet.2016.06.126

21. Soares AF, Tatumi SH, Mazzo TM, Rocca RR, Courrol LC (2017) Study of morphological and luminescent properties (TL and OSL) of ZnO nanocrystals synthetized by coprecipitation method. J Lumin 186:135–143. https://doi.org/10.1016/j.jlumin.2017.02.028

22. Chen Y-Y, Kuo C-C, Chen B-Y, Chiu P-C, Tsai P-C (2015) Multifunctional polyacrylonitrile-ZnO/Ag electrospun nanofiber membranes with various ZnO morphologies for photocatalytic, UV-shielding, and antibacterial applications. J Polym Sci Part B Polym Phys 53:262–269. https://doi.org/10.1002/polb.23621

23. Byzynski G, Melo C, Volanti DP, Ferrer MM, Gouveia AF, Ribeiro C, Andrés J, Longo E (2017) The interplay between morphology and photocatalytic activity in ZnO and N-doped ZnO crystals. Mater Des 120:363–375. https://doi.org/10.1016/j.matdes.2017.02.020

24. Zhao S, Zhang YW, Zhou YM, Sheng XL, Zhang C, Zhang MY, Fang JS (2016) One-step synthesis of core-shell structured mesoporous silica spheres templated by protic ionic liquid and CTAB. Mater Lett 178:35–38. https://doi.org/10.1016/j.matlet.2016.04.182

25. Noda A, Susan AB, Kudo K, Mitsushima S, Hayamizu K, Watanabe M (2003) Brønsted acid−base ionic liquids as proton-conducting nonaqueous electrolytes. J Phys Chem B 107:4024–4033. https://doi.org/10.1021/jp022347p

26. Bijad M, Karimi-Maleh H, Khalilzadeh MA (2013) Application of ZnO/CNTs nanocomposite ionic liquid paste electrode as a sensitive voltammetric sensor for determination of ascorbic acid in food samples. Food Anal Methods 6:1639–1647. https://doi.org/10.1007/s12161-013-9585-9

27. Taherkhani JT, Hadadzadeh H, Karimi-Maleh H, Beitollahi H, Taghavi M, Karimi F (2014) ZnO nanoparticle-modified ionic liquid-carbon paste electrode for voltammetric determination of folic acid in food and pharmaceutical samples. Ionics 20:421–429. https://doi.org/10.1007/s11581-013-0992-0

28. Straumal BB, Protasova SG, Mazilkin AA, Goering E, Schütz G, Straumal PB, Baretzky B (2016) Ferromagnetism of zinc oxide nanograined films. J Nanotechnol 7:1936–1947. https://doi.org/10.1134/S0021364013060143

29. Cassol CC, Ebeling G, Ferrera B, Dupont J (2006) A simple and practical method for the preparation and purity determination of halide-free imidazolium ionic liquids. Adv Synth Catal 348:243–248. https://doi.org/10.1002/adsc.200505295

30. Rietveld HM (1967) Line profiles of neutron powder-diffraction peaks for structure refinement. Acta Cryst 22:151–152. https://doi.org/10.1107/S0365110X67000234

31. Larson AC, Von Dreele RB (2004) General Structure Analysis System (GSAS). Los Alamos National Laboratory Report LAUR 86–748. http://11bm.xray.aps.anl.gov/documents/GSASManual.pdf.

32. Badawy MI, Ali MEM, Ghaly MY, El-Missiry MA (2015) Mesoporous simonkolleite–TiO$_2$ nanostructured composite for simultaneous photocatalytic hydrogen production and dye decontamination. Process Saf Environ 94:11–17. https://doi.org/10.1016/j.psep.2014.12.001

33. Kim K-S, Demberelnyamba D, Lee H (2004) Size-selective synthesis of gold and platinum nanoparticles using novel thiol-functionalized ionic liquids. Langmuir 20:556–560. https://doi.org/10.1021/la0355848

34. Montenegro DN, Hortelano V, Martínez O, Martínez-Tomas MC, Sallet V, Munoz-Sanjosé V, Jimenez J (2013) Non-radiative recombination centres in catalyst-free ZnO nanorods grown by atmospheric-metal organic chemical vapour deposition. J Phys D Appl Phys 46:235302. https://doi.org/10.1088/0022-3727/46/23/235302

35. Zhang R, Yin PG, Wang N, Guo L (2009) Photoluminescence and Raman scattering of ZnO nanorods. Solid State Sci 11:865–869. https://doi.org/10.1016/j.solidstatesciences.2008.10.016

36. Dodd AC, Mckinley AJ, Saunders M, Tsuzuki T (2006) Effect of particle size on the photocatalytic activity of nanoparticulate zinc oxide. J Nanopart Res 8:43–51. https://doi.org/10.1007/s11051-005-5131-z

37. Otsuka M (2004) Comparative particle size determination of phenacetin bulk powder by using Kubelka–Munk theory and principal component regression analysis based on near-infrared spectroscopy. Powder Technol 141:244–250. https://doi.org/10.1016/j.powtec.2004.01.025

38. Yi S, Zhao F, Yue X, Wang D, Lin Y (2015) Enhanced solar light-driven photocatalytic activity of BiOBr–ZnO heterojunctions with effective separation and transfer properties of photo-generated chargers. New J Chem 39:6659–6666. https://doi.org/10.1039/C5NJ00707K

39. Pal M, Bera S, Jana S (2015) Sol–gel based simonkolleite nanopetals with SnO$_2$ nanoparticles in graphite-like amorphous carbon as an efficient and reusable photocatalyst. RSC Adv 5(92):75062–75074. https://doi.org/10.1039/c5ra12322d

40. Mazzo TM, Oliveira LMR, Macario LR, Avansi W Jr, André RS, Rosa ILV, Varela JA, Longo E (2014) Photoluminescence properties of CaTiO3:Eu^{3+} nanophosphor obtained by the polymeric precursor method. Mater Chem Phys 145:141–150. https://doi.org/10.1016/j.matchemphys.2014.01.051

41. Longo VM, Cavalcante LS, Erlo R, Mastelaro VR, de Figueiredo AT, Sambrano JR, de Lázaro S, Freitas AZ, Gomes L, Vieira ND Jr, Varela JA, Longo E (2008) Strong violet−blue light photoluminescence emission at room temperature in SrZrO$_3$: joint experimental and theoretical study. Acta Mater 56:2191–2202. https://doi.org/10.1016/j.actamat.2007.12.059

42. Roy N, Roy A (2015) Growth and temperature dependent photoluminescence characteristics of ZnO tetrapods. Ceram Int 41:4154–4160. https://doi.org/10.1016/j.ceramint.2014.11.113

43. Lin B, Fu Z, Jia Y, Liao G (2001) Defect photoluminescence of undoping ZnO films and its dependence on annealing conditions. J Electrochem Soc 148:110–113. https://doi.org/10.1149/1.1346616

44. Sithole J, Ngom BD, Khamlich S, Manikanadan E, Manyala N, Saboungi ML, Knoessen D, Nemutudi R, Maaza M (2012) Simonkolleitenano-platelets: synthesis and temperature effect on hydrogen gas sensing properties. Appl Surf Sci 258:7839–7843. https://doi.org/10.1016/j.apsusc.2012.04.073

45. Yun HJ, Lee H, Joo JB, Kim W, Yi J (2009) Influence of aspect ratio of TiO_2 nanorods on the photocatalytic decomposition of formic acid. J Phys Chem C 113:3050–3055. https://doi.org/10.1021/jp808604t

46. La Porta FA, Andres J, Vismara MVG, Graeff CFO, Sambrano JR, Li MS, Varela JA, Longo E (2014) Correlation between structural and electronic order–disorder effects and optical properties in ZnO nanocrystals. J Mater Chem C 2:10164–10174. https://doi.org/10.1039/C4TC01248H

47. Zheng P, Pan Z, Li H, Bai B, Guan W (2015) Effect of different type of scavengers on the photocatalytic removal of copper and cyanide in the presence of TiO_2@yeast hybrids. J Mater Sci Mater Electron 26:6399–6410. https://doi.org/10.1007/s10854-015-3229-3

48. Chen H, Zhu L, Liu H, Li W (2013) $Zn_5(OH)_8Cl_2$·H_2O-based quantum dots-sensitized solar cells: a common corrosion product enhances the performance of photoelectrochemical cells. Electrochim Acta 105:289–298. https://doi.org/10.1016/j.electacta.2013.04.175

49. Moniem SMA, Ali MEM, Gad-Allah TA, Khalil ASG, Ulbricht M, El-Shahat MF, Ashmawy AM, Ibrahim HS (2015) Detoxification of hexavalent chromium in wastewater containing organic substances using simonkolleite-TiO_2 photocatalyst. Process Saf Environ 95:247–254. https://doi.org/10.1016/j.psep.2015.03.010

50. Khan M, Naqvi AH, Ahmad M (2015) Comparative study of the cytotoxic and genotoxic potentials of zinc oxide and titanium dioxide nanoparticles. Toxicol Rep 2:765–774. https://doi.org/10.1016/j.toxrep.2015.02.004

51. Tong Y, Yang H, Li J, Yang Y (2013) Extraction of Au(III) by ionic liquid from hydrochloric acid medium. Sep Purif Technol 120:367–372. https://doi.org/10.1016/j.seppur.2013.10.028

52. Tanaka H, Fujioka A, Futoyu A, Kandori K, Ishikawa T (2007) Synthesis and characterization of layered zinc hydroxychlorides. J Solid State 180:2061–2066. https://doi.org/10.1016/j.jssc.2007.05.001

53. Qu Q, Yan C, Wan Y, Cao C (2012) Effects of NaCl and SO_2 on the initial atmospheric corrosion of zinc. Corros Sci 44:2789–2803. https://doi.org/10.1016/S0010-938X(02)00076-8.

54. Dai T-F, Hsu W-C, Hsu H-C (2014) Improvement of photoluminescence and lasing properties in ZnO submicron spheres by elimination of surface-trapped state. Opt Express 22:27169–27174. https://doi.org/10.1364/OE.22.027169

55. Kim W, Choi M, Yong K (2015) Generation of oxygen vacancies in ZnO nanorods/films and their effects on gas sensing properties. Sensors Actuators B Chem 209:989–996. https://doi.org/10.1016/j.snb.2014.12.072

56. Kim CH, Kim B-H (2015) Zinc oxide/activated carbon nanofiber composites for high-performance supercapacitor electrodes. J Power Sources 274:512–520. https://doi.org/10.1016/j.jpowsour.2014.10.126

57. Meng F, Ge F, Chen Y, Xu G, Huang F (2018) Local structural changes induced by ion bombardment in magnetron sputtered ZnO: Al films: Raman, XPS, and XAS study. Surf Coat Technol. https://doi.org/10.1016/j.surfcoat.2018.04.013